X-Ray Near-Field Ptychography for Optically Thick Specimens

Marco Stockmar,* Irene Zanette, Martin Dierolf, Bjoern Enders, Richard Clare, and Franz Pfeiffer
Lehrstuhl für Biomedizinische Physik, Physik-Department and Institut für Medizintechnik, Technische Universität München, 85748 Garching, Germany

Peter Cloetens and Anne Bonnin†
European Synchrotron Radiation Facility (ESRF), 38043 Grenoble, France

Pierre Thibault
Department of Physics and Astronomy, University College London, London WC1E 6BT, United Kingdom
(Received 15 September 2014; revised manuscript received 18 December 2014; published 21 January 2015)

Inline holography, like other lensless imaging methods, circumvents limitations of x-ray optics through an *a posteriori* phase-retrieval step. However, phase retrieval for optically thick, i.e., strongly absorbing and phase shifting, specimens remains challenging. In this paper, we demonstrate that near-field ptychography can be used to efficiently perform phase retrieval on a uranium sphere with a diameter of about 46 μm, which acts as an optically thick sample. This particular sample was not accessible by inline holography previously. The reconstruction is based on a statistical model and incorporates partial coherence by decomposing the illumination into coherent modes. Furthermore, we observe that phase vortices, which can occur as artifacts during the reconstruction, pose a greater challenge than in far-field methods. We expect that the methods described in this paper will allow production of reliable phase maps of samples which cannot be accessed by inline holography.

DOI: 10.1103/PhysRevApplied.3.014005

I. INTRODUCTION

Full-field phase-contrast imaging techniques based on x-ray propagation are now routinely used in a range of disciplines like biomedical science [1], paleontology [2], and materials science [3]. These techniques, which generally do not require image-forming optics, can be complemented with a phase-retrieval step to provide quantitative maps of the complex-valued transmission function of a sample. Unlike their far-field counterparts [4–6], propagation-based imaging techniques operate in the Fresnel regime and therefore benefit from lower requirements in detector dynamic range and in beam coherence. Imaging optically thick, i.e., strongly absorbing and phase shifting, objects at high spatial resolution with inline holography remains challenging when phase retrieval is based on a linearization of the sample transmission function [7]. Different methods such as the mixed approach [8] and transport of intensity equation (TIE) [9–11] address this challenge. All of these approaches have been designed to require the illuminating wave front to be free of strong distortions. Slowly varying inhomogeneities can be corrected by dividing the diffraction patterns by a flat field, an image of the empty beam without the sample. Nevertheless, division by a flat field does not account for the wave nature of x rays where strong inhomogeneities in the illumination copropagate with the waves diffracted by the sample, resulting in reconstruction artifacts mainly at high resolutions [12,13].

Ptychographic phase retrieval [14–16] solves the aforementioned problem by simultaneously retrieving the complex-valued illumination function, in this field commonly called "probe," along with the complex-valued sample transmission function.

Recently, two approaches were reported that transferred this concept to the regime of inline holography. Robisch and Salditt used a ptychographic phase-retrieval scheme on a series of diffraction patterns recorded on multiple sample-to-detector distances [17]. The other technique, coined "near-field ptychography," acquires multiple diffraction patterns at a single sample-to-detector distance, but with different transverse positions of the sample relative to a nonhomogeneous or structured illumination [18].

In this paper, we show that near-field ptychography efficiently solves the issues associated with strongly absorbing and phase-shifting specimens. Solving those aforementioned issues makes the technique truly versatile and allows us to overcome the limitations of other inline holographic methods.

II. METHODS AND MATERIALS

A. Near-field ptychography

In near-field ptychography, a series of diffraction patterns $I_j(\vec{r})$ is recorded while the sample $\tau(\vec{r}-\vec{r}_j)$ is

*marco.stockmar@ph.tum.de
†Present address: Paul Scherrer Institut, Swiss Light Source, CH-5232 Villigen, Switzerland.

scanned to different relative transverse positions $\vec{r}_j = (x_j, y_j)$ with respect to the incident illumination $\psi(\vec{r})$. The intensity recorded on the detector placed at a distance z from the sample is given by

$$I_j(\vec{r}) = |\mathcal{D}[\chi_j(\vec{r})]|^2, \tag{1}$$

where

$$\chi_j(\vec{r}) = \psi(\vec{r})\tau(\vec{r} - \vec{r}_j) \tag{2}$$

describes the exit wave directly behind the sample and

$$\mathcal{D}_z[\chi(\vec{r})] = \mathcal{F}^{-1}\left[\mathcal{F}[\chi(\vec{r})]e^{iz\sqrt{k^2-\vec{q}^2}}\right] \tag{3}$$

is called the angular spectrum propagator, in which k is the wave number and $\mathcal{F}$ denotes the two-dimensional Fourier transform with reciprocal-space coordinate $\vec{q} = (q_x, q_y)$ [19].

Complementarity in the measured diffraction patterns can be obtained if the incident illumination diverges from a homogeneous wave front. Divergence from a homogeneous wave front can be achieved, for example, by using a static random-phase screen which introduces high-contrast structures in the illumination while minimizing absorption [18].

Furthermore, Eq. (1) can be modified to incorporate partial coherence using the coherent-mode formulation of Wolf [20], which decomposes the illumination function into mutually incoherent modes. Existing phasing algorithms can be modified to work in this mixed-state formulation and to reconstruct a finite number of coherent modes $\psi^l(\vec{r})$ along with the sample image [21],

$$I_j(\vec{r}) = \sum_l |\mathcal{D}_z[\chi_j^l(\vec{r})]|^2 = \sum_l |\mathcal{D}_z[\psi^l(\vec{r})\tau(\vec{r} - \vec{r}_j)]|^2. \tag{4}$$

B. Sample description

The sample of interest in this experiment is a uranium-molybdenum spherical particle with a 46 μm outer diameter glued to the top of a capillary. It is made of a U-7Mo (7 wt.% Mo) core, produced by atomization methods, and protected by a 1-μm-thick UO_2 shell [22]. At 16.9 keV, this sample absorbs in its center almost 95% of the incoming intensity and yields a phase shift of more than 10π, thus violating assumptions of slowly varying phase and weak absorption. With this strong phase shift, the dense sphere acts as a diverging lens. This particular sample could not be imaged with other inline holography methods because it was impossible to carry out a proper flat-field normalization [13,23].

This U-Mo alloy dispersed in an aluminum matrix is the most promising high-density nuclear fuel needed to decrease the uranium enrichment of current nuclear fuels for research and test reactors worldwide [24]. To optimize performance during in-reactor irradiation, the growth of an interaction layer at the uranium-aluminum interface has to be avoided [25]. One way to succeed consists in coating the U-Mo particles with a protective layer made of UO_2 [24,26]. The efficiency of such a coating is directly linked to its microstructural homogeneity such as uniformity of thickness and the absence of cracks.

C. Experimental implementation

The experiment was carried out at the standard magnified holotomography setup of the nanoimaging end station of beam line ID22 at the European Synchrotron Radiation Facility (ESRF) in Grenoble, France [27]. Figure 1(a) shows a sketch of the setup. The incoming radiation from the undulator located 64 m away was focused to a virtual source with a FWHM of about 80 nm by a pair of crossed Kirkpatrick-Baez (KB) mirrors. The detector consists of a lens-coupled CCD (FReLoN) with 2048^2 pixels, 14-bit dynamic range, and an effective detector pixel size of $\Delta s = 0.756$ μm. The sample was placed downstream of the focal point at $z_1 = 5.19$ cm. The distance between focal point and detector was $L = 52.523$ cm. Rescaling to a parallel beam geometry [28] results in a magnification of $M = L/z_1 = 10.12$ and an effective pixel size of $\Delta x = \Delta s/M = 74.75$ nm. The resulting effective propagation distance is then $z = (L - z_1)/M = 4.68$ cm. To add additional structures in the illuminating wave front, a static diffuser consisting of a piece of cardboard was placed

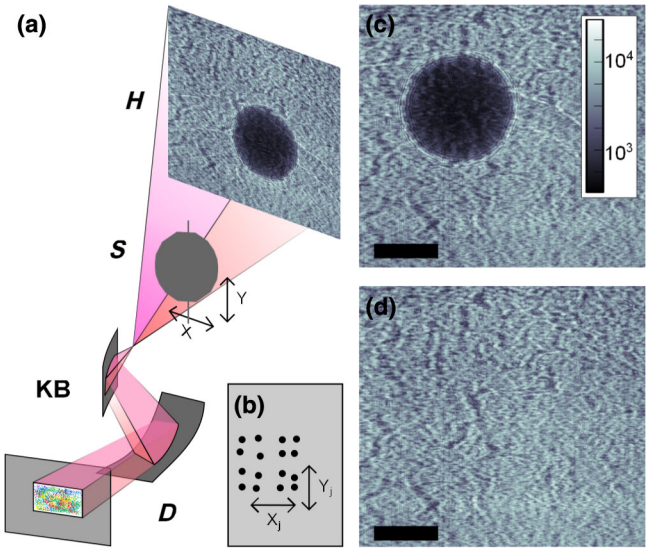

FIG. 1. (a) Experimental implementation, where D denotes the diffuser, KB denotes the pair of KB mirrors, S denotes the sample and H denotes the hologram recorded on the detector. (b) Scanning scheme used. (c) One of the 16 holograms with the sample visible at the top left of the image. (d) Hologram of the empty beam. Note that the intensities measured in detector counts are plotted on a logarithmic scale due to the high dynamic range within the images. One detector count corresponds to approximately three photons. The scale bars correspond to 15 μm.

directly upstream of the KB mirrors. The mean energy was about 16.96 keV with a bandwidth of about 2%. For the application of a likelihood model, which will be discussed in the next subsection [see Eqs. (5) and (6)], we have used the fact that one detector count corresponds to approximately $f_I = 3$ photons.

To suppress raster-grid artifacts [29], one ptychographic scan consisted of 16 pseudorandomly distributed points with a maximum shift of 350 pixels. At each point, a diffraction pattern of 2048^2 pixels was acquired using an exposure time of 0.5 s. Five flat images, i.e., frames without the sample, were recorded as well.

All diffraction patterns were corrected by subtracting the dark current and deconvolving the detector point-spread function measured in a previous experiment using five iterations of the Richardson-Lucy algorithm [30,31].

D. Reconstruction of experimental data

The reconstruction is based on the model for the diffracted intensity described in Eq. (4). The ptychographic reconstruction algorithms search for the desired quantities τ and $\psi^l(\vec{r})$, which solve the system of equations defined by Eq. (4). In this work, two different algorithms were used.

The difference-map algorithm interprets Eqs. (2) and (4) as two constraint sets. The two constraint sets naturally define two projection operators and the solution, which is the intersection of both sets, is found by a scheme of alternating projections onto these sets. More details can be found elsewhere [18,32]. The additionally recorded flat images were used to further suppress raster-grid artifacts and to support the reconstruction of the illumination function [29].

The maximum-likelihood algorithm assumes that the measured intensity in each pixel of the diffraction pattern is the result of a Gaussian random process with a standard deviation of

$$\sigma_j(\vec{r}) = \sqrt{f_I I_j(\vec{r})}, \tag{5}$$

where $f_I I_j(\vec{r})$ is the number of photons in the detector pixel at position $\vec{r}$. The reconstruction problem can then be described by finding the ψ^l and τ which maximize the probability for the measured data $I_j(\vec{r})$ by minimizing the following negative log-likelihood function:

$$L(\tau,\psi^l) = \sum_j \sum_{\vec{r}} \frac{1}{\sigma_j(\vec{r})^2} \Big[\sum\nolimits_l |\mathcal{D}_z[\psi^l(\vec{r})\tau(\vec{r}-\vec{r}_j)]|^2 - f_I I_j(\vec{r}) \Big]^2 + \alpha \sum_{\vec{r}} |\nabla\tau(\vec{r})|^2. \tag{6}$$

The last term in Eq. (6) is a regularization term with an amplitude α which imposes a penalty on strong fluctuations within the sample. The search is carried out by a nonlinear conjugate gradient implementation as described in detail in Ref. [33].

The reconstruction was carried out in three steps with the difference-map algorithm and the maximum-likelihood algorithm:

In the first step, 1000 iterations of the difference-map algorithm using only a single mode for the illumination function were used. To avoid numerical instabilities at places of strong absorption during the reconstruction, the absolute value of the sample transmission function was forced to remain within the interval [0.1,1.2]. This clipping constraint is a common strategy in iterative phase retrieval (e.g., in Ref. [34]). With the chosen boundaries, it is a rather weak constraint and should in practice not restrict the applicability of the method provided sufficient transmitted intensity in the diffraction data. Moreover, this clipping constraint was not used in the final maximum likelihood refinement.

In the second step, two additional modes [see Eq. (4)] were added to the illumination function to account for partial coherence as well as the remaining inconsistencies in the measured data. These additional modes were initialized as random arrays and 300 iterations of the difference-map algorithm were performed.

The third and final step consisted of 300 iterations of the maximum-likelihood algorithm. This refinement step was found to reduce artifacts and noise in the final reconstruction.

III. RESULTS AND DISCUSSION

The result of the procedure described above is shown in Fig. 2. The main mode of the reconstructed illumination corresponds well to a former experiment with the same diffuser and similar experimental conditions, where a well-known test object was used [18]. Because the numerical propagation of the wave fields is based on discrete Fourier transforms, artifacts are produced along the boundaries of the field of view. Due to the near-field geometry, unlike when using a far-field geometry, the illumination is allowed to extend the field of view of the reconstruction since diffraction acts locally on the length scale of a Fresnel zone $\sqrt{\lambda z} = 1.85\ \mu$m, which corresponds to approximately 25 pixels [35]. Boundary effects due to an extended illumination function will occur on the same length scale. Moreover, the reconstruction of the illumination is only well constrained where the sample is. The two additional modes in the illumination function took up about 5% of the power each (after orthogonalization). Besides being a model for partial coherence, these modes can account for the point-spread function and nonuniform response of the detector. More generally speaking, the additional modes add additional degrees of freedom to the reconstruction. In this way, they pick up not only illumination characteristics but general inconsistencies [36,37] between the measured data and the rigid model [Eq. (1)] assumed for reconstruction. Hence, an exact physical

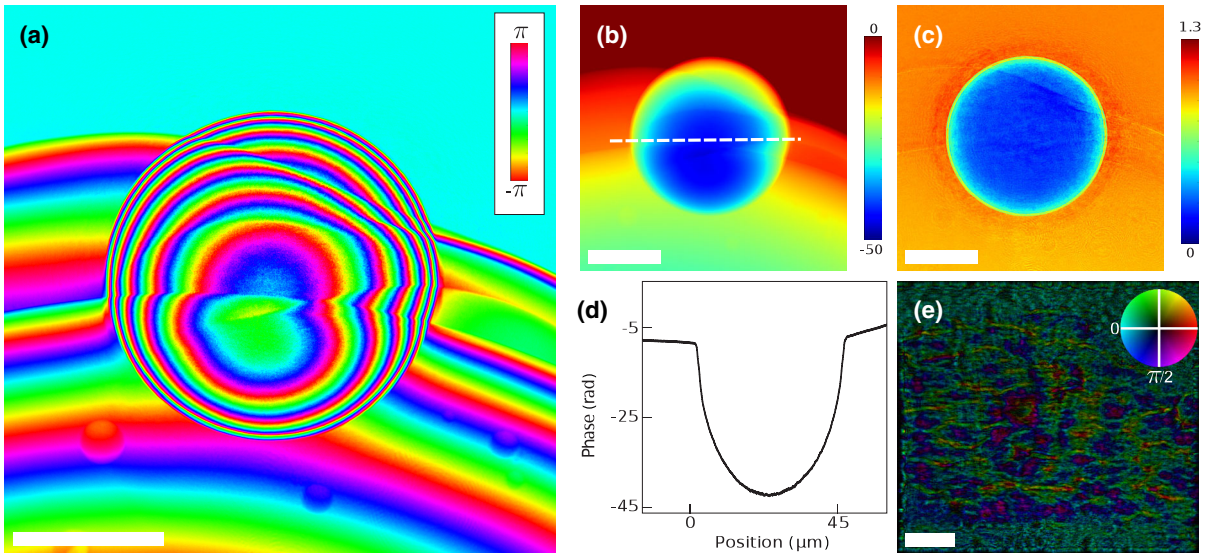

FIG. 2. Ptychographic reconstruction results. (a) Phase part of the reconstructed transmission function. (b) Same as (a) after unwrapping. (c) Amplitude of the reconstructed transmission function. (d) Line profile through (b) as indicated by the dashed line. (e) Representation of the main mode of the complex-valued illumination function, where the phase and amplitude are mapped respectively to hue and intensity. The scale bars correspond to 25 μm.

interpretation of each single mode is not always possible and depends on the source of signal degradation.

The phase image of the sample [Fig. 2(a)] shows that the uranium sphere and the surrounding glue both exhibit a strong phase shift. The measured phase shift in the center of the sphere after subtracting the glue background can be estimated to be 33.6 rad, which is in good agreement with the expected value based on data obtained from Ref. [38]. The phase error of the surrounding air is estimated from the standard deviation to 0.012 rad. The outer UO_2 shell cannot be distinguished from the U-7Mo core, which can be attributed to the small thickness and the fact that contrast is washed out in two dimensions due to the line-integral effect. The amplitude image [Fig. 2(c)] shows that the sphere attenuates the amplitude of the incident wave down to 15%. We also notice that it contains ringing artifacts which appear on the interfaces between glue, air, and sphere and are clearly visible as a halo around the sphere.

The experiment described so far was repeated for different viewing angles of the sample, which rotated around the vertical axis. The sample transmission function obtained after the first step in the ptychographic reconstruction often required the removal of phase vortices before the last two steps could be executed. While phase vortices [28] in the illumination may very well occur, such singularities are highly unlikely in an object transmission function. Figure 3 shows two different types of vortices that could be observed: in Fig. 3(a) a pair of vortices with opposite helicity is shown. Figure 3(b) shows a single vortex. The vortices are located close to the center of the sphere and have a nearly vanishing amplitude in their core (much lower than the surrounding pixels; not depicted in the figure). The occurrence of phase vortices during the reconstruction process is not unusual [39], but most of the vortices merge with or annihilate other vortices while building up the phase. However, unlike in far-field methods, in the near-field case, the vortices only result in local inconsistencies with the measured data, therefore strongly reducing the algorithm's efficacy at removing them. While it is possible that a pair of vortices as in Fig. 3(a) annihilates spontaneously after a sufficient number of iterations, single vortices as in Fig. 3(b) are global dislocations which are effectively pinned within the low-transmission area close to the center of the sphere. These vortices cannot heal on their own because the iterative algorithms do not provide a sufficient driving force to drag them towards the edge of the image, where they could annihilate. Fortunately, the occurrence of these vortices, the position of their core

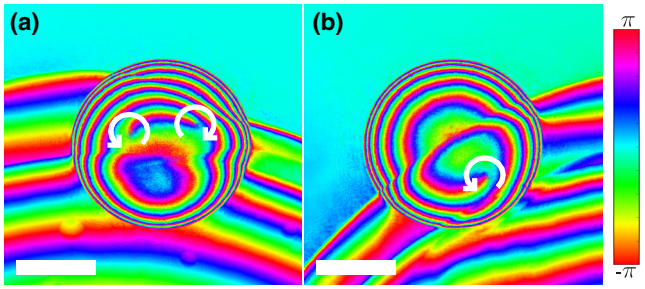

FIG. 3. Vortices can occur as artifacts in the reconstruction. (a) Phase image of a pair of phase vortices with opposite helicities. (b) A single vortex trapped close to the center of the sphere (reconstruction from a data set taken after the sample had been rotated). The scale bars correspond to 20 μm.

(x_v, y_v), and their helicity m can be easily determined upon visual inspection after step one of the reconstruction procedure. Eventually, they can be removed through multiplication with a vortex of opposite helicity,

$$v(\vec{r}) = \exp\left[-im \arctan\left(\frac{x - x_v}{y - y_v}\right)\right]. \quad (7)$$

This operation produces a local error around the core, which is corrected by carrying out 100 additional difference-map iterations before proceeding with step two in the reconstruction procedure.

IV. SUMMARY AND CONCLUSIONS

This paper demonstrates the potential of near-field ptychography as a versatile methodology to obtain quantitative images even of strongly absorbing and phase-shifting objects. As with far-field ptychography, it was found that using a mixed-state approach improved noticeably the quality of the reconstruction. The *local* nature of Fresnel diffraction patterns makes more likely the occurrence of pinned phase vortices, which can however be removed reliably.

Near-field ptychography will achieve its full potential when combined with tomography. First tests indicate that the number of iterations can be greatly reduced when the output of one ptychographical reconstruction is fed as the initial guess for the reconstruction of a projection taken at a neighboring angle. Another important future direction is to investigate ways to reduce artifacts in the absorption image. An absorption image with reduced artifacts would allow us to obtain complementary quantitative information which is especially valuable in studies of heterogeneous specimens. Moreover, investigations on the convergence properties for the algorithms used in this work and for other ptychographic algorithms which could be modified for near-field ptychography should be carried out. Furthermore, it should be possible to detect and remove vortices automatically by using the fact that cross-derivatives of the phase are not equal at a singularity.

ACKNOWLEDGMENTS

We acknowledge financial support through the DFG Cluster of Excellence Munich-Centre for Advanced Photonics (MAP), the DFG Gottfried Wilhelm Leibniz program, the European Research Council (ERC, Starting Grant OptImaX), and the TUM Graduate School.

[1] M. Langer, A. Pacureanu, H. Suhonen, Q. Grimal, P. Cloetens, and F. Peyrin, X-ray phase nanotomography resolves the 3D human bone ultrastructure, PLoS One **7**, e35691 (2012).

[2] P. Tafforeau, R. Boistel, E. Boller, A. Bravin, M. Brunet, Y. Chaimanee, P. Cloetens, M. Feist, J. Hoszowska, J.-J. Jaeger, R. F. Kay, V. Lazzari, L. Marivaux, A. Nel, C. Nemoz, X. Thibault, P. Vignaud, and S. Zabler, Applications of x-ray synchrotron microtomography for non-destructive 3D studies of paleontological specimens, Appl. Phys. A **83**, 195 (2006).

[3] S. C. Mayo, A. W. Stevenson, and S. W. Wilkins, In-line phase-contrast x-ray imaging and tomography for materials science, Materials **5**, 937 (2012).

[4] J. Miao, P. Charalambous, and J. Kirz, Extending the methodology of x-ray crystallography to allow imaging of micrometre-sized non-crystalline specimens, Nature (London) **400**, 342 (1999).

[5] S. Eisebitt, J. Lüning, W. F. Schlotter, M. Lörgen, O. Hellwig, W. Eberhardt, and J. Stöhr, Lensless imaging of magnetic nanostructures by x-ray spectro-holography, Nature (London) **432**, 885 (2004).

[6] B. Abbey, K. A. Nugent, G. J. Williams, J. N. Clark, A. G. Peele, M. A. Pfeifer, M. de Jonge, and I. McNulty, Keyhole coherent diffractive imaging, Nat. Phys. **4**, 394 (2008).

[7] P. Cloetens, W. Ludwig, J. Baruchel, D. Van Dyck, J. Van Landuyt, J. P. Guigay, and M. Schlenker, Holotomography: Quantitative phase tomography with micrometer resolution using hard synchrotron radiation x rays, Appl. Phys. Lett. **75**, 2912 (1999).

[8] J. P. Guigay, M. Langer, R. Boistel, and P. Cloetens, Mixed transfer function and transport of intensity approach for phase retrieval in the Fresnel region, Opt. Lett. **32**, 1617 (2007).

[9] K. A. Nugent, T. E. Gureyev, D. F. Cookson, D. Paganin, and Z. Barnea, Quantitative phase imaging using hard x rays, Phys. Rev. Lett. **77**, 2961 (1996).

[10] S. C. Mayo, P. R. Miller, S. W. Wilkins, T. J. Davis, D. Gao, T. E. Gureyev, D. Paganin, D. J. Parry, A. Pogany, and A. W. Stevenson, Quantitative x-ray projection microscopy: Phase-contrast and multi-spectral imaging, J. Microsc. **207**, 79 (2002).

[11] M. Krenkel, M. Bartels, and T. Salditt, Transport of intensity phase reconstruction to solve the twin image problem in holographic x-ray imaging, Opt. Express **21**, 2220 (2013).

[12] R. Mokso, P. Cloetens, E. Maire, W. Ludwig, and J.-Y. Buffèire, Nanoscale zoom tomography with hard x rays using Kirkpatrick-Baez optics, Appl. Phys. Lett. **90**, 144104 (2007).

[13] J. Hagemann, D. R. Luke, C. Homann, T. Hohage, P. Cloetens, H. Suhonen, and T. Salditt, Reconstruction of wave front and object for inline holography from a set of detection planes, Opt. Express **22**, 11552 (2014).

[14] P. Thibault, M. Dierolf, A. Menzel, O. Bunk, C. David, and F. Pfeiffer, High-resolution scanning x-ray diffraction microscopy, Science **321**, 379 (2008).

[15] M. Guizar-Sicairos and J. R. Fienup, Phase retrieval with transverse translation diversity: A nonlinear optimization approach, Opt. Express **16**, 7264 (2008).

[16] A. M. Maiden and J. M. Rodenburg, An improved ptychographical phase-retrieval algorithm for diffractive imaging, Ultramicroscopy **109**, 1256 (2009).

[17] A. Robisch and T. Salditt, Phase retrieval for object and probe using a series of defocus near-field images, Opt. Express **21**, 23345 (2013).
[18] M. Stockmar, P. Cloetens, I. Zanette, B. Enders, M. Dierolf, F. Pfeiffer, and P. Thibault, Near-field ptychography: Phase retrieval for inline holography using a structured illumination, Sci. Rep. **3**, 1927 (2013).
[19] J. W. Goodman, *Introduction to Fourier Optics*, 3rd ed. (Roberts & Company Publishers, Englewood, Colorado, 2005).
[20] A. Starikov and E. Wolf, Coherent-mode representation of Gaussian Schell-model sources and of their radiation fields, J. Opt. Soc. Am. **72**, 923 (1982).
[21] P. Thibault and A. Menzel, Reconstructing state mixtures from diffraction measurements, Nature (London) **494**, 68 (2013).
[22] A. Bonnin, J. P. Wright, R. Tucoulou, and H. Palancher, Impurity precipitation in atomized particles evidenced by nano x-ray diffraction computed tomography, Appl. Phys. Lett. **105**, 084103 (2014).
[23] See the Supplemental Material at http://link.aps.org/supplemental/10.1103/PhysRevApplied.3.014005 for a demonstration on how the flat-field correction fails with this sample.
[24] A. Leenaers, S. Van den Berghe, E. Koonen, C. Jarousse, F. Huet, M. Trotabas, M. Boyard, S. Guillot, L. Sannen, and M. Verwerft, Post-irradiation examination of uranium 7 wt% molybdenum atomized dispersion fuel, J. Nucl. Mater. **335**, 39 (2004).
[25] H. Palancher, A. Bonnin, V. Honkimäki, H. Suhonen, P. Cloetens, T. Zweifel, R. Tucoulou, A. Rack, and M. Voltolini, Coating thickness determination in highly absorbent coreshell systems, J. Appl. Crystallogr. **45**, 906 (2012).
[26] M. K. Meyer, G. L. Hofman, S. L. Hayes, C. R. Clark, T. C. Wiencek, J. L. Snelgrove, and R. V. Strain, Low-temperature irradiation behavior of uranium-molybdenum alloy dispersion fuel, J. Nucl. Mater. **304**, 221 (2002).
[27] G. Martínez-Criado, R. Tucoulou, P. Cloetens, P. Bleuet, S. Bohic, J. Cauzid, I. Kieffer, E. Kosior, S. Labouré, S. Petitgirard, A. Rack, J. A. Sans, J. Segura-Ruiz, H. Suhonen, J. Susini, and J. Villanova, Status of the hard x-ray microprobe beamline ID22 of the European Synchrotron Radiation Facility, J. Synchrotron Radiat. **19**, 1 (2011).
[28] D. Paganin, *Coherent X-Ray Optics*, Oxford Series on Synchrotron Radiation (Oxford University Press, New York, 2006).
[29] M. Dierolf, P. Thibault, A. Menzel, C. M. Kewish, K. Jefimovs, I. Schlichting, K. V. König, O. Bunk, and F. Pfeiffer, Ptychographic coherent diffractive imaging of weakly scattering specimens, New J. Phys. **12**, 035017 (2010).
[30] W. H. Richardson, Bayesian-based iterative method of image restoration, J. Opt. Soc. Am. **62**, 55 (1972).
[31] L. B. Lucy, An iterative technique for the rectification of observed distributions, Astron. J. **79**, 745 (1974).
[32] P. Thibault, M. Dierolf, O. Bunk, A. Menzel, and F. Pfeiffer, Probe retrieval in ptychographic coherent diffractive imaging, Ultramicroscopy **109**, 338 (2009).
[33] P. Thibault and M. Guizar-Sicairos, Maximum-likelihood refinement for coherent diffractive imaging, New J. Phys. **14**, 063004 (2012).
[34] R. N. Wilke, M. Priebe, and M. Bartels, Hard x-ray imaging of bacterial cells: Nano-diffraction and ptychographic reconstruction, Opt. Express **20**, 19232 (2012).
[35] *Principles of Optics: Electromagnetic Theory of Propagation, Interference and Diffraction of Light*, edited by M. Born and E. Wolf, 7th ed. (Cambridge University Press, Cambridge, England, 1999).
[36] B. Enders, M. Dierolf, P. Cloetens, M. Stockmar, F. Pfeiffer, and P. Thibault, Ptychography with broad-bandwidth radiation, Appl. Phys. Lett. **104**, 171104 (2014).
[37] J. N. Clark, X. Huang, R. J. Harder, and I. K. Robinson, Dynamic imaging using ptychography, Phys. Rev. Lett. **112**, 113901 (2014).
[38] B. L. Henke, E. M. Gullikson, and J. C. Davis, X-ray interactions: Photoabsorption, scattering, transmission, and reflection at $E = 50$–$30\,000$ eV, $Z = 1$–92, At. Data Nucl. Data Tables **54**, 181 (1993).
[39] J. R. Fienup, C. C. Wackerman, and A. Arbor, Phase-retrieval stagnation problems and solutions, J. Opt. Soc. Am. A **3**, 1897 (1986).